

Alma Mater Studiorum Università di Bologna
Archivio istituzionale della ricerca

An Ultra-low Power Ultra-wide Bandwidth Positioning System

This is the final peer-reviewed author's accepted manuscript (postprint) of the following publication:

Published Version:

Dardari, D., Decarli, N., Guerra, A., Fantuzzi, M., Masotti, D., Costanzo, A., et al. (2020). An Ultra-low Power Ultra-wide Bandwidth Positioning System. IEEE JOURNAL OF RADIO FREQUENCY IDENTIFICATION, 4(4), 353-364 [10.1109/JRFID.2020.3008200].

Availability:

This version is available at: <https://hdl.handle.net/11585/772506> since: 2021-10-04

Published:

DOI: <http://doi.org/10.1109/JRFID.2020.3008200>

Terms of use:

Some rights reserved. The terms and conditions for the reuse of this version of the manuscript are specified in the publishing policy. For all terms of use and more information see the publisher's website.

This item was downloaded from IRIS Università di Bologna (<https://cris.unibo.it/>).
When citing, please refer to the published version.

(Article begins on next page)

This is the post peer-review accepted manuscript of:

D. Dardari et al., "An Ultra-Low Power Ultra-Wide Bandwidth Positioning System," in IEEE Journal of Radio Frequency Identification, vol. 4, no. 4, pp. 353-364, Dec. 2020, doi: 10.1109/JRFID.2020.3008200.

The published version is available online at: <https://ieeexplore.ieee.org/document/9137221>

© 2020 IEEE. Personal use of this material is permitted. Permission from IEEE must be obtained for all other uses, in any current or future media, including reprinting/republishing this material for advertising or promotional purposes, creating new collective works, for resale or redistribution to servers or lists, or reuse of any copyrighted component of this work in other works

An Ultra-low Power Ultra-wide Bandwidth Positioning System

Davide Dardari, Nicolò Decarli, Anna Guerra, Marco Fantuzzi, Diego Masotti, Alessandra Costanzo *DEI-CNIT, Università degli Studi di Bologna, Cesena, Italy* - {name.surname}@unibo.it
 Davide Fabbri, Aldo Romani *DEI-ARCES, Università degli Studi di Bologna, Cesena, Italy* - {name.surname}@unibo.it
 Maxime Drouguet, Thomas Feuillen, Christopher Raucy, Luc Vandendorpe, Christophe Craeye *ICTEAM Institute, Université catholique de Louvain, Louvain-la-Neuve, Belgium* - {name.surname}@uclouvain.be

Abstract—An ultra-wide bandwidth (UWB) remote-powered positioning system for potential use in tracking floating objects inside space stations is presented. It makes use of battery-less tags that are powered-up and addressed through wireless power transfer in the UHF band and embeds an energy efficient pulse generator in the 3-5 GHz UWB band. The system has been mounted on the ESA Mars Rover prototype to demonstrate its functionality and performance. Experimental results show the feasibility of centimeter-level localization accuracy at distances larger than 10 meters, with the capability of determining the position of multiple tags using a 2W-ERP (Effective Radiated Power) power source in the UHF RFID frequency band.

Index Terms—Ultra-wide bandwidth (UWB), positioning, wire-less power transfer, pulse generation, space stations

I. INTRODUCTION

In recent years we have assisted to an increasing interest in localizing objects and persons equipped with low-cost battery-less tags in indoor environments. The targeted applications are in the fields of logistics, retail, security, etc. [1].

The UHF Gen.2 RFID technology standard is currently the most popular solution for item identification. Unfortunately, it has been primarily designed for identification rather than positioning. So commercial readers can only obtain position information. Some approaches have been proposed to improve significantly the localization accuracy [2]–[5], for instance, by exploiting phase measurements. Unfortunately, they require expensive hardware at the reader side (e.g., large antenna arrays) or are extremely sensitive to multipath and phase ambiguities. Which means that they may be not reliable when working in harsh propagation environments. .

At the same time, some new real-time locating systems (RTLS) have emerged, providing high-accuracy localization by adopting ultra-wide bandwidth (UWB) signals and exploiting their fine time resolution capabilities [6]. Nevertheless, current UWB-based localization systems make use of active tags with a current consumption larger than 50 mA, which is not compatible with the exploitation of energy harvesting or wireless power transfer techniques, so that batteries or extremely low duty-cycle operations are unavoidable [7].

This work was supported in part by the European Space Agency, under Contract ESA AO 1-8471/15/NL/LvH, and in part by the European Union's Horizon 2020 Research and Innovation Programme under the Marie Skłodowska-Curie under Grant 793581.

Recently, following the same backscattering philosophy as in standard Gen.2 RFID systems, some solutions have been proposed to realize battery-less tags working with UWB backscattered signals, achieving interesting results in terms of positioning accuracy (in the 5-15 cm range) [8]–[15]. Despite its promising characteristics in terms of low-complexity and low-power consumption, the backscatter-based architecture suffers from strong link-budget (2-way link due to the reflected signal) which, in addition to the very conservative power-emission regulation in the UWB band, limits its application only to very-short range scenarios (typically below 10 meters) [16].

In this paper, which is an extended version of [17], we illustrate a RTLS with ultra-low power tags capable of extending the range even beyond 10 meters by using energy efficient UWB pulse generators and energy harvesting. After the description of the main functional blocks of the system, experimental results are presented. The system has been developed within the project “LOST” (Localisation of Objects in Space through RF Tags) funded by the ESA (European Space Agency). The purpose of LOST was to investigate suitable technologies to localize objects deployed or floating inside the International Space Station or future space stations. Such an “indoor” space application is aimed at tracking every tagged object present in the environment to avoid potential dangerous situations and to allow astronauts not to waste their extremely valuable time searching lost tools or to take care of instruments used by astronauts who left the platform.

II. SYSTEM REQUIREMENTS AND ARCHITECTURE

The requirements of the LOST project were very challenging, especially regarding the target localization accuracy (close to 1 cm) and coverage (> 10 meters). Both of which are in contrast with the need of having battery-less tags, and the utilization of off-the-shelf components (i.e., no integrated circuits design). In a nutshell, power is delivered to the tag through a UHF link, which is modulated to provide basic commands. The tag then transmits a UWB pulse, captured by the receiving nodes, which send the samples to a central unit, where correlations are computed, providing time-difference-of-arrival (TDOA) information, which are then exploited to locate the tag.

A. General Architecture

- *The Central Unit* is a software module running on a general-purpose computer. It is in charge of: (i) scheduling the addressing of each tag in the area by sending proper commands to the Reference Nodes and the Power Transfer Units; (ii) collecting the TDOA measurements from the Reference Nodes; (iii) estimating the position of each tag (localization engine); (iv) managing the entire network (configuration, calibration, diagnosis, etc.); (v) providing an application program interface to the Graphical User Interface (GUI). The position estimation and tracking algorithm makes use of a particle filter [6].
- *The Graphical User Interface* is a software module that provides the user with a graphical representation of tag positions through continuous interrogations of the Central Unit.
- *The Power Transfer Unit* (“energy shower”) is a customized module which transmits RF energy in the UHF band to all tags in the area. Furthermore, according to the scheduling set by the Central Unit, it sends periodically a specific ON-OFF keying (OOK) modulated signal to address the tags in turn.
- *The Control Interface* translates the commands received from the Control Unit through the network into a sequence of hardware commands with digital outputs driving the other blocks of the LOST system. That module consists of a microcontroller equipped with an Ethernet interface and/or a Wi-Fi interface with several digital outputs. It has been implemented using the general-purpose Raspberry Pi board equipped with both interfaces and general-purpose digital outputs (GPIO). The control interface is accompanied by a 100 MHz reference oscillator for clock distribution to the reference nodes.
- *The Tag* which, according to the requirements, should be battery-less and harvest the necessary energy from the RF signal emitted by the Power Transfer Units (see Sec. III). Once addressed, the tag wakes up for a short time to provide a feedback to the Reference Nodes by generating a quasi-periodic sequence of UWB pulses.

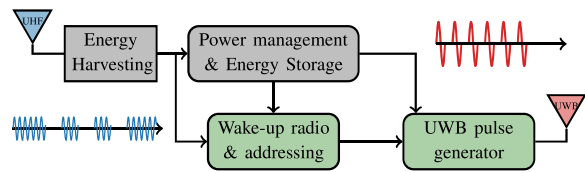


TABLE I
BLOCKS COMPOSING THE SYSTEM AND THEIR COMMERCIAL
COMPONENTS

	Key Hardware	Sect.	Detail
Central Unit	Computer		Intel Core i7 or equivalent
Power Transfer Unit	UHF Generator	IIIa	HopeRF RFM23BP
	Power Amplifier	IIIa	RFMD RF6886
	UHF Antenna	IIIa	Abracon Technology ARRSN5 or ARRTN5
Control Interface	Microcontroller		Raspberry PI 3
	Reference Clock	V	Cristek CPRO33-100, Texas Instr. CDCLVC1310
Tag	UHF Rectenna	IIIb	Custom Designs
	Power management	IIIc	Texas Instr. BQ25575
	Wake-up Radio	IIIc	RFMD RF6886
	UWB Generator	IV	[19]
	UWB Antenna	V	[18]
UWB Synch TX	UWB Generator	IV	[19]
	UWB Antenna	V	[18]
Reference Node	UWB Antenna	V	[18] or [20]
	LNA	V	Mini-Circuits ZX60-63LN, Macom MAAL-011078
	Filter	V	Custom 5th order hairpin
	ADC	V	Texas Instr. ADC12J4000
	FPGA	V	Altera Arria V GZ

- *The reference nodes* which acquire the UWB sequence generated by the tag. There are at least three of them; they forward the data to the Central Unit where the TDOA is estimated through proper algorithms as detailed in Sec. VI.
- *The UWB Synch TX node* (not shown in figure) provides a general synchronization signal for calibration purposes. Moreover, the presence of this reference synchronization signal enables the introduction of TDOA estimation schemes robust to clock offset and drift (see Sec. VI).

B. Working Principle

The area to be monitored is equipped with N_{rx} receiving reference nodes. Their number is chosen to guarantee a sufficient service coverage in the intended area in terms of tag detectability and localization accuracy. The LOST system is controlled by the Central Unit that periodically initiates an interrogation cycle in which a specific tag is addressed via the

UHF link. Specifically, at the beginning of the interrogation cycle, the intended tag is addressed (i.e., woken up) by sending its ID through the UHF link, modulating the UHF carrier using an OOK scheme. Between consecutive interrogation cycles, a UHF continuous wave signal is emitted by the Power Transfer Units (energy showers) to let all tags in the area collect a sufficient amount of energy to operate when addressed. Once woken up, the tag emits a sequence of UWB pulses and returns to a sleep mode, waiting for the next interrogation cycle. During the transmission of the UWB pulses sequence, all Reference Nodes are triggered to perform analog-to-digital conversion and buffering. The received samples are then forwarded to the Central Unit that is in charge of detecting the tag and of computing the TDOAs between the signals received by different Reference Nodes. The localization engine, running in the Central Unit, combines all TDOA measurements to estimate the position of the tag. The tags present in the area are addressed sequentially through successive interrogation cycles. Between consecutive interrogation cycles, each Reference Node performs the necessary processing tasks of the samples recorded in its buffer. To allow sufficient energy to be transferred to the tags, the time interval is longer than the duration of interrogation itself. Operating in this way allows the processing speed to be slightly relaxed with respect to an actual real-time implementation.

III. WIRELESS POWER TRANSFER

A. Energy showers

Fig. 3 shows a schematics of the Power Transfer Unit. The baseband OOK signal, coming from the Control Interface, is connected to the modulation input of the UHF generator (RFM23BP board from HOPERF Electronic). In order to avoid harmonic distortion coming from the UHF generator, the transmission power was set to (+10 dBm). Hence, an optional limiter has been introduced after the generator to prevent damage to the power amplifier input (RF6886 from RFMD), which is in charge to increase the power up to 2 Watt. Then a low pass filter insures harmonic rejection (in our case mainly coming from the UHF generator rather than from the distortion of the power amplifier). Finally, the signal reaches the antenna (ARRSN5 or ARRTN5 from Abracon Technology). Those antennas were chosen for their low directivity and circular polarization, ensuring the proper Energy Shower functionality. The resulting signal is a 2 Watt Effective Radiated Power (ERP) signal at 868 MHz, considering that the gain of the antenna balances the cable and filter losses. Fig. 4 is a picture of the Power Transfer Unit.

B. Rectenna

A preliminary investigation in [21] on the expected performance of standard rectennas at 868 MHz and 2.45 GHz has been carried out. Which showed that, despite the more compact antenna structure at higher frequencies, the European Gen2 RFID frequency band of 868 MHz is preferable when stringent distance coverage is requested, such as in the LOST project, where a 10 m source-tag distance is considered. As a first trial, a single monopole rectenna was tested, in order

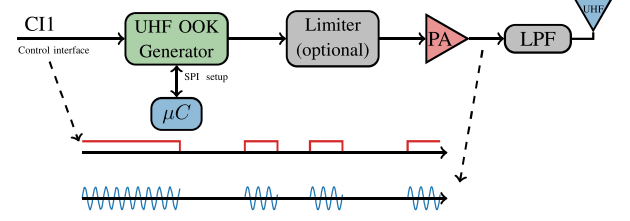


Fig. 3. Schematics of the energy shower sub-system.

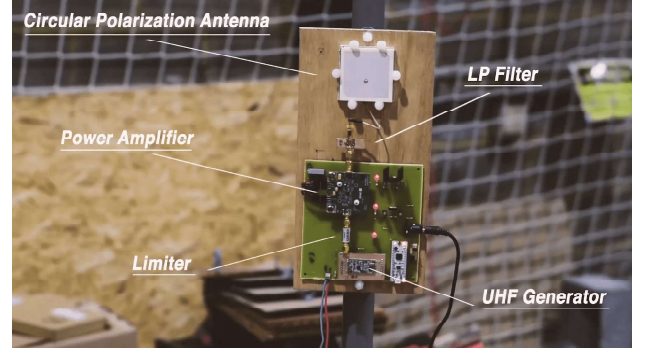


Fig. 4. Picture of the energy-shower sub-system.

to verify the need for a *cold-start* of the PMU [22]. In Fig. 5 the corresponding prototype is presented. This initial design enabled to successfully test the circuit architecture described later on. Because of its linear polarization, the capability to efficiently receive just a portion of the incoming signal is limited. To overcome this, an orientation-independent behaviour is targeted, thus leading to a multi-antenna solution for the UHF radiating part of the rectenna. A dual-monopole layout with horizontal and vertical placements, thus theoretically able to capture almost any polarized incoming field [22], was chosen. Fig. 6 shows a picture of the whole prototype: the two planar meandered monopoles (on a 0.5-mm-thick Rogers RO4350B substrate with $\epsilon_r = 3.48$, $\tan(\delta) = 0.0037$ at 10 GHz) resonate at 868 MHz.

Additionally, the power from the two antennas are not combined at RF, UHF in this case, but in DC, after rectification. Therefore, the proposed solution is an array of two rectennas, each one with its own rectifying section, rather than a single rectenna with an array of antennas [23]. As a further distinct feature, the two rectennas have a dual rectification path, as can be evinced by the schematic view of Fig. 7: the main upper path provides the needed energy to a DC/DC converter, supporting the UWB pulse chip while the lower one manages the WUR (lumped components reported in Tab. II). Then, the DC outputs of all individual antennas are connected in series in order to sum up their voltages. This solution is accomplished through an almost lossless capacitive divider [24]: and the power sent by the energy showers is directly split at RF by that reactive-only network.

Of course, the presence of the WUR path alters the loading condition of the rectifier path (and vice-versa) and has to be taken into account during the optimization process: here, the main goal has been not to affect the main harvesting

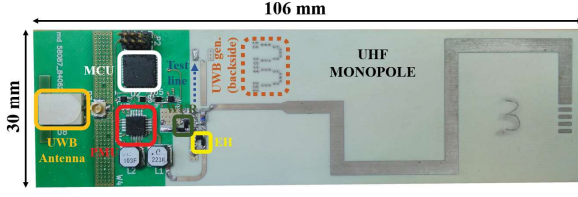


Fig. 5. The initial single-monopole UHF/UWB tag prototype.

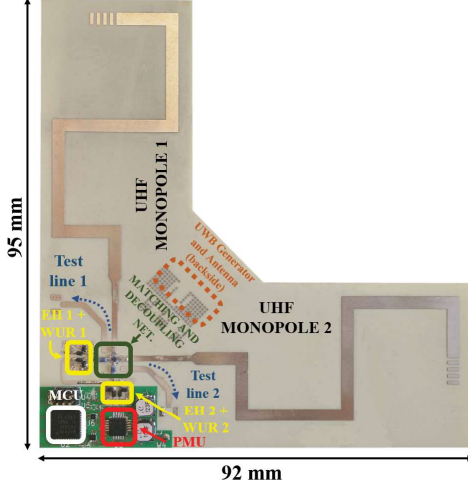


Fig. 6. The implemented dual-monopole UHF/UWB tag.

operation of the rectifier path. Nonetheless, we stress that the WUR path does not require the delivery of any relevant amount of power, but it rather provides information through the demodulated signal. The effectiveness of the adopted solution is demonstrated in Fig. 8, by the preliminary results of the power splitting between the two paths as function of the WUR load (which will significantly change during the charging operation): as can be seen from Fig. 8(a), the main rectifier operation is almost insensitive to the WUR load variation, as needed.

The most demanding task in the design process of the presented multi-rectenna has been the RF decoupling of the very close monopoles. In Fig. 6, the RF ports of the two antennas are $\lambda/20$ apart, and this leads to a strong electromagnetic coupling between the antennas, thus having a twofold impact on the overall rectenna performance: i) a distorted radiation pattern of each monopole, far from being omnidirectional in the desired plane; ii) a significant interference between the two ports in terms of accepted signal, whose effect is a priori unpredictable. For this reason, a strategic role is played by the lumped-element decoupling network (see Fig. 7) [22], whose role is to guarantee each rectenna to operate as if it was standalone.

As regards to the UWB localization capability of the tag, this is possible through the presence of a miniaturized UWB chip antenna on-board (or external antennas) and a UWB pulse generator IC (in Fig. 5, 6 their footprints are highlighted). One can also note that multi-mode solutions with a single UWB/UHF antenna are also available [21]. In this way, a more compact layout is achieved, at the expense of reduced

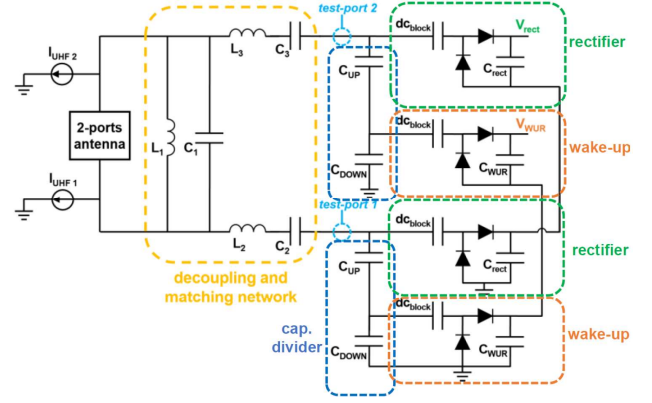


Fig. 7. Circuit schematic of the two-monopole rectenna with decoupling/matching network.

TABLE II
DUAL-MONOPOLE RECTENNA LUMPED COMPONENT VALUES. CC = COILCRAFT, MT = MURATA AND SKW = SKYWORKS.

Name	L_1	C_1	$L_2 = L_3$	$C_2 = C_3$	C_{up}	C_{down}	DC_{block}	$D_1 - D_4$	C_{rect}	C_{WUR}
Value	56 nH	2.8 pF	27 nH	39 pF	0.7 pF	1 pF	10 pF	SMS	10 pF	10 pF
Man.	Cc	Mt	Cc	Mt	Mt	Mt	ATC	Skw	Mt	Mt

harvesting performance. Additionally, the adopted solution of the on-board UWB pulse generator, described in Section IV, can be further improved by deploying a less energy-hungry solution: the nonlinear rectifying operation is fruitfully exploited in [25], where multi-sine energy showers in the UHF band produce a high number of intermodulation products falling in the UWB band, thus providing automatically a quasi-UWB pulse.

As a final detail on the rectenna optimization, it is worth noticing that the rectenna is described as a whole system by means of electromagnetic/nonlinear co-design strategies [26]. In this way, the optimization process can consider different incoming power levels as well as the dispersive behaviour of the antenna and the unavoidable interaction between the RF and the DC sections of the system. As mentioned at the beginning of this subsection, the more stringent “cold start” condition of the PMU is considered as a goal during the design: for the adopted PMU (TI bq25570) it corresponds to a DC voltage $V_{th}=330$ mV and a rectified power $P_{th}=15$ μ W. The final multi-rectenna performance are given in Fig. 9 where a 2-W ERP circularly polarized emitting UHF source is placed at different distances from the tag and the corresponding (simulated) rectified power and voltage are retrieved. The plots show that the “cold-start” constraints (horizontal dashed lines) are satisfied. It is worth mentioning that the most stringent constraint is represented by the power threshold. Superimposed to these plots, there are also few measured data (red markers) which are in good agreement with predictions.

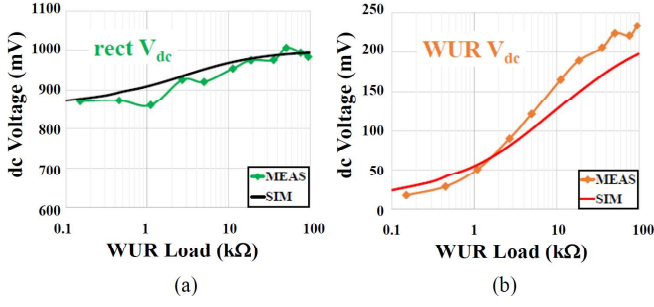


Fig. 8. Comparison between measured and modeled dc voltage at (a) the rectifier and (b) WUR outputs vs. the WUR load (input power of -13 dBm) for the dual-monopole rectenna.

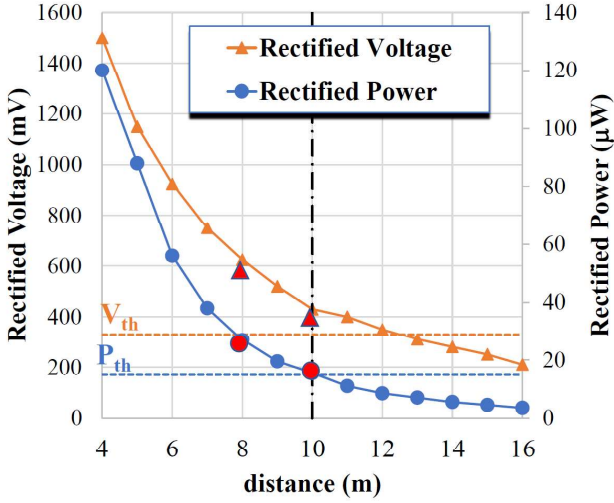


Fig. 9. Double-monopole rectenna rectified voltage and power, for different distance from a 2-W ERP circularly polarized energy shower. The red markers represent measured data which confirm the predicted trend.

C. Power Management and Wake-up Radio

The block diagram of the PMU, along with the WUR and the control circuitry are depicted in Fig. 10. Components and architectures were chosen to minimize the quiescent power consumption and the overall consumed energy, as described in detail in [27]. The PMU is composed of a bq25570 regulated DC/DC converter from Texas Instruments (TI), which also performs a fractional open-circuit voltage maximum power point tracking of the RF source. The DC/DC converter integrates a voltage monitor that is used to control the power supply to the microcontroller unit (MCU) depending on the harvested energy, which must be sufficient to power at least an entire addressing phase and a UWB transmission. The rectified signal from the WUR path of the rectenna is sent to a WUR inspired by [28] and based on a TLV3691 comparator, which detects the OOK modulation by the RF source and decodes the tag address with the aid of a MCU. The WUR outputs a digital signal containing the 10-bit tag address (data rate 2.2 Kbit/sec) sent by the Power Transfer Unit that is decoded by the ultra-low power MSP430 MCU from TI. An external low drop-out regulator MCP1711 with ultra-low quiescent current is supplied with the same voltage by the control

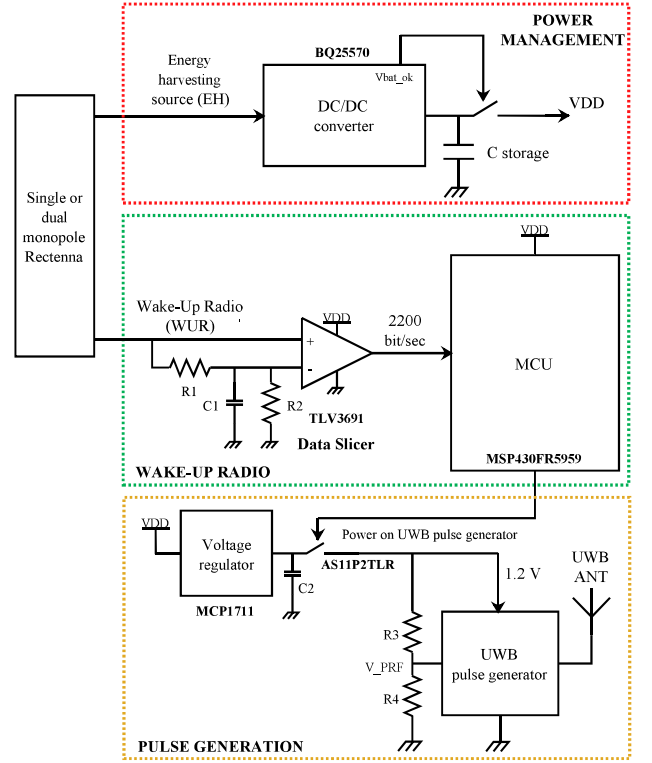


Fig. 10. Base-band circuit structure of the proposed tag.

circuit and is used to power the UWB pulse generator. An analog switch controlled by the MCU connects or disconnects the UWB pulse generator depending on the level of energy stored internally by the tag during the energy harvesting phase. Additional tests were carried on by replacing the PMU with the nano-current ASIC described in [29], which operates with lower quiescent current and lower minimum required input voltage, as described in the numerical results (Tab. IV).

IV. ULTRA-LOW POWER UWB GENERATOR

Both the tags and the UWB Synch TX node are based on an experimental IC developed at UCLouvain [19]. This IC contains two UWB generators, one of which has a tunable PRF (Pulse Repetition Frequency) and is exploited in this system. Fig. 11 shows the generator board.

The IC is controlled through its main supply. When the IC operates as a tag, the ignition is managed by the MCU with an analog switch which is closed when the tag is addressed. When the IC is operated as a Sync TX node, the ignition is managed by the control interface through a direct connection. In both cases, the PRF is set with a resistive divider, providing DC bias voltage to the generator.

The pulse generator itself (Fig. 11) has been borrowed from the authors of [19]. The circuit is based on a 65 nm CMOS technology. It includes a voltage controlled ring oscillator, a buffer and a pulse shaping filter. A control voltage (V_{CTRL_DIV}) is used to set the Pulse Repetition Frequency. The generator's energy consumption is close to 1.5 pJ per pulse. Fig. 12 shows the relationship between V_{CTRL_DIV} ,



Fig. 11. UWB generator.

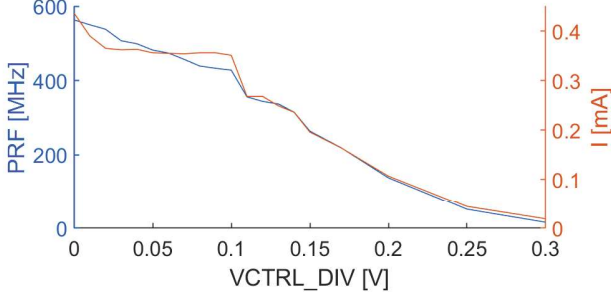


Fig. 12. PRF and Current as a function of VCTRL_DIV input.

the PRF and the IC current consumption at 1.2V supply voltage. The working point is near 0.17 V, yielding a PRF of approximately 200 MHz for a current consumption around $160\mu A$ while the IC is powered on. Fig. 13 shows a typical pulse measured at the output of the IC, with and without the anti-aliasing RF bandpass filter. This measurement has been carried out with the 50 Ohm load of the a high-performance oscilloscope (Keysight DSOX91604A). The output pulses are truncated leading to an important output power limitation and to high DC content in the pulse. Therefore, a 19 dB externally powered amplifier has been used. Nevertheless, a new generator has been recently developed by the same team, with excellent spectral occupancy and much higher peak-to-peak level, such that new (probably even better) localization experiments could be carried out without an amplifier.

The generator presents a strong jitter in pulse repetition frequency. The generated burst of pulses can be modeled as

$$s(t) = \sum_{n=0}^{N_s-1} g(t - nT_f - \epsilon_n), \quad (1)$$

where N_s is the number of pulses, T_f is the (average) pulse repetition period, and ϵ_n are random variables modeling the time jitter. Usually the jitter is an unwanted effect, but in this case it helps to reduce the level of side lobes in the auto-correlation function. We will show in Sec. VI that the ambiguity in TDOA estimation is mitigated.

V. RECEIVING NODES

Fig. 14 shows a picture of a reference node. Starting from the antenna on top, it is easy to recognize the front end, followed by the ADC and FPGA buffer (the LAN interface is not shown). The antenna [18] corresponds to an evolution of the UWB Circular Disc Monopole antenna [30], which has

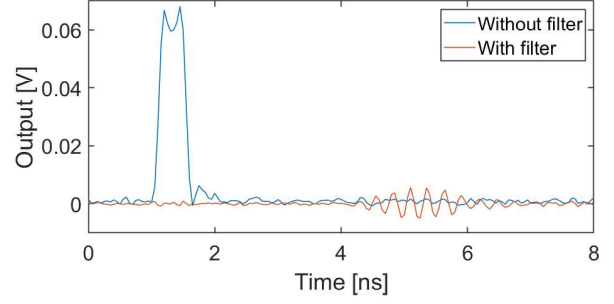


Fig. 13. Measured output pulses.

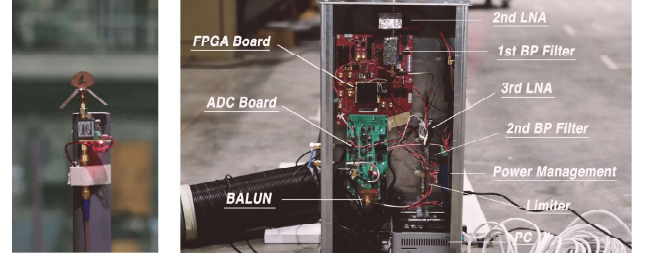


Fig. 14. Reference node. Left: antenna, first LNA and its bias tee. Right: second and third LNAs, filters, limiter, balun, ADC and FPGA.

been previously used for positioning applications. However, at higher frequencies, the pattern of this antenna does not remain omnidirectional in azimuth and it tends to shift upward. Reference [18] proposes new structures for both the monopole radiator and the ground plane in order to stabilize the radiation pattern. The full disk now becomes a sector of disk and the ground plane is a narrow rectangular structure bent downward at about 45 degrees. The maximum horizontal extent of the antenna is limited to 5.5 cm. If the positioning must take place in a highly-reflecting environment, those omni-directional antennas are replaced by traveling-wave antennas, inspired from Vivaldi antennas, made of a half tapered-slot antenna standing above a folded ground plane. This allows directional radiation without the need for a balun. The radiation pattern has a width of almost 90 degrees in the horizontal plane which is ideal for observation of a rectangular field of view from the corners of a room. That alternative antenna and its radiation patterns are shown in Fig. 15.

Each block of the front-end (see Fig. 16) has been measured. Also, the ADC and associated FPGA functionalities have been tested regarding buffering, synchronisation, and triggering performance. Measurements and results are described below. The first LNA (ZX60-83LN+ from Mini-Circuits) has a noise figure of 1.6 dB, while the second and third LNAs (MAAL-011078 from Macom, mounted on a custom board) have a noise figure higher than 1.31 dB, with an average value near 1.16 dB. The gain of the first LNA is 21 dB while the second and third LNAs is 19 dB average.

Fig. 17 shows the performance of the two filters placed respectively after the second and third LNAs. The measured curve exhibits a sharp filtering in the desired band (see Fig. 17). As this filter also acts as an antialiasing filter, we have designed it in order to achieve a transmission coefficient

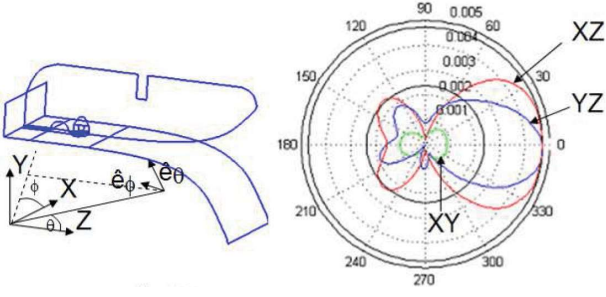


Fig. 15. From [20]. Left: hybrid tapered-slot antennas. Right: radiation patterns in three principal planes.

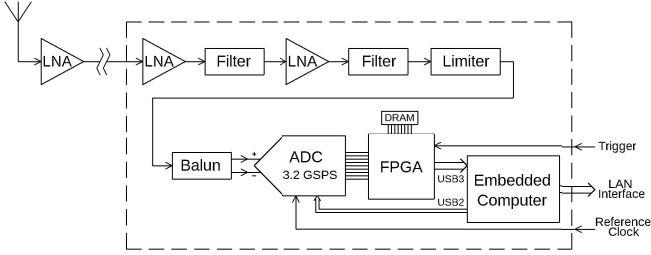


Fig. 16. Reference node. Block diagram.

at the limit frequencies (3.2 and 4.8 GHz). It was also important to have sufficient rejection in the 2.4 GHz ISM band. The resulting filter (designed and simulated with the help of Keysight ADS software) is a 5th-order Hairpin Filter in microstrip technology.

After the LNAs and filters, comes a limiter (VLM-63-2W from Mini-Circuits) devoted to protection of the ADC input. Tests have been carried out while the LNAs were saturated (either with continuous-wave or pulsed signals). It appeared that the limiter works as stated in its datasheet. Since the limiting value was a little too high, sufficient cable length has been placed after it, such that the signals get slightly attenuated. The ADC follows, after a balun (balanced-to-unbalanced) circuit. In this setup, the balun needs to split the power of the unbalanced signal in two paths and with a phase difference of 180 degrees. Balance is ensured within less than one dB, the reflection coefficient is better than -10 dB, with a value below -20 dB near the center of the useful band. The maximum ADC (ADC12J400 from Texas Instruments) maximum sampling rate is 4 Gs/sec; it is set here to 3.2 Gs/sec. The nominal number of bits is 12, with 8 to 9 effective bits in the frequency range of interest. Their -3dB analog bandwidth is 3.2 GHz. The ADCs are controlled through an FPGA (also from TI). In the current application, ADCs of the different reference nodes are synchronized through a coaxial connection to a 100 MHz reference clock (CPRO33-100.000 from crystek Crystals and CDCLVC1310EVM from Texas Instruments).

The ADCs, controlled with an FPGA, have been tested in many different ways, one of which consisted in feeding two reference nodes with the same signal and check if the correlation between the two sampled signals is as expected. This test aimed to check the synchronization of the clocks, the proper response to the trigger and the data consistency

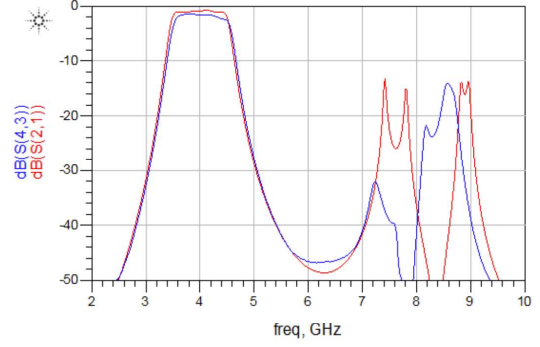


Fig. 17. Response of the filter of the reference node. The useful band is between 3 and 5 GHz.

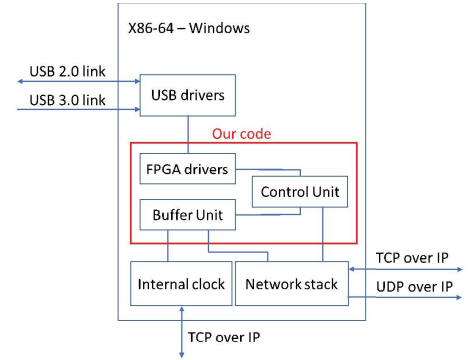


Fig. 18. Client block diagram.

after sub-sampling and buffering. To this end, the UWB pulse generator was connected to the two front end through a power splitter and several attenuators.

Data transfer at sufficient rate presents a real challenge. The FPGA and ADC boards are connected with two USB links to the x86-64 client. Each client is connected to a LAN with an Ethernet cable. The x86-64 server is also connected to the LAN. The commands are sent into the network through a TCP/IP connection while the measurements are sent over a UDP/IP link. The TCP connection ensures proper verification of the packets transfer, while the UDP maximizes the data throughput. The code running inside the client (see Fig. 18) is composed of three different parts. The first one consists of all the drivers necessary to communicate with the modules inside the FPGA. The second part consists of a buffer management system. It adds the identity of the reference node and the time of the measurement. The internal clock of the client is synchronized with an accuracy of 200 μ s to a time server placed on the LAN. This means that tag interrogations must be spaced by more than 400 μ s in order to eliminate the ambiguity between data packets received at the server. The last part is the control unit that manages the overall client code.

The data packet streamed by the client to the server contains raw data, node ID and timestamp (the latter two being negligible given the throughput). Let us assume a tag's signal lasts 41 μ s, which corresponds to 2^{17} samples at the ADC rate of 3.2 Gs/sec. This amount of data appears twice (tag to be localized and calibration tag). Besides that, one should account for 100 μ s of maximum latency of the tag response

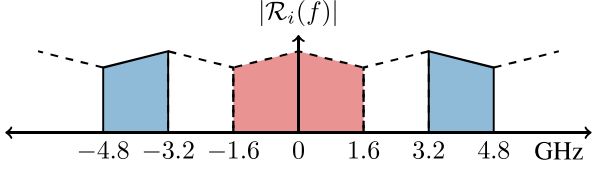


Fig. 19. Spectrum produced by the UWB pulse generator (solid lines and blue) and the aliased versions after sampling at sub-Nyquist rate (dotted). The red aliased version is the one sampled by the ADCs.

and three 10 μ s period between different operations, bringing the total duration of data to 212 μ s. Since each sample is coded on 2 Bytes, that leads to 1.36 MB to be transferred at each localization and from each reference node.

VI. SIGNAL PROCESSING

The signal generated by the UWB pulse generator is compliant with the standardized UWB emission mask [31]. Therefore it is of the bandpass type with its emitted power located between 3.2 and 4.8 GHz respectively. Such a spectral content enables the acquisition of the signal with a sub-Nyquist sampling rate which reduces the complexity of the ADC process. Indeed, as shown in Fig. 19, provided that the signal is sampled at precisely 3.2 Gs/sec, the aliased repetitions located between -1.6 and 1.6 GHz will be fully acquired. For the rest of the discussion this recorded signal will be referred as the *low-frequency* signal.

As will be described later, a key operation to be performed at the receiver side is the cross-correlation operation required to estimate the TDOAs between pairs of receiving nodes. Let us denote by $r_i[n]$ the sampled signal received at node i at the rate $1/T_s = 3.2$ Gs/sec. The TDOA $n_{ij}T_s$ between receiving nodes i and j is obtained by finding the index n_m which maximizes the cross-correlation function between these two nodes, that is:

$$n_{ij} = \operatorname{argmax}_{n_m} C_{ij}[n] = \operatorname{argmax}_{n_m} \sum_{n=-\infty}^{\infty} r_i[n] r_j[n - n_m]. \quad (2)$$

Directly applying the correlation on this *low-frequency* signal will lead to a correlation function exhibiting two impairments. Firstly, the inherent resolution of the bandpass pulse will be lost because of the *low-frequency* content, resulting in a broader correlation peak. Indeed, authors in [32] showed that both the bandwidth and the carrier frequency play an important role in the curvature of the correlation function. Secondly, the relatively low sampling rate of 3.2 Gs/sec will generate an accuracy of around 5 cm which is insufficient for the considered application. Thus, some processing has to be applied to this *low-frequency* signal leveraging the structure of the aliased signal with respect to the carrier frequency to obtain a satisfactory correlation accuracy.

As is well-known, the spectrum $C_{ij}(f)$ associated with $C_{ij}[n]$ is given by

$$C_{ij}(f) = \mathcal{R}_i(f) \mathcal{R}_j^*(f), \quad (3)$$

where $\mathcal{R}_i(f)$ is the Fourier transform of signal $r_i[n]$. From (3) it is clear that the spectral content of the cross-correlation function is located at the intersection of the spectral content of signals $r_i[n]$ and $r_j[n]$. If these two signals have similar spectral locations, so will their cross-correlation function. The consequence of sub-Nyquist sampling is that the original spectrum content is repeated and is, for positive (resp. negative) frequencies, basically shifted from the range $[3.2, 4.8]$ GHz (resp. $[-4.8, -3.2]$ GHz) to the range $[0, 1.6]$ GHz (resp. $[-1.6, 0]$ GHz). To benefit from the properties of the signals sent by the UWB transmitter, the spectral content of the signal or of their corresponding cross-correlation functions has to be shifted back. This process actually corresponds to the interpolation of a signal by means of a bandpass filter. The minimum sampling rate at which the final result can be obtained is $3/T_s = 9.6$ Gs/s. Once the spectral content is back to its original position, further interpolation (without any spectral shift) can be achieved by additional zero padding, so that the correlation function can be obtained at, for instance, 38.4 or 76.8 Gs/s. Doing the correlation using first the *low-frequency* signal and then shifting it to the correct band also leads to substantial gain in processing time. Indeed, this first cross-correlation requires less computing power because of the relatively low sampling rate. Using this, the rest of the high resolution processing can be performed only on a specific region of interest. In our case, given the integration time and the sampling frequency, the correlation is computed for delays corresponding to ranges up to 10 km. Knowing that the actual delay is realistically below 100 m, we can discard the rest of the data and process only the relevant ones. This results in a computing time gain that allows the set-up to work in real-time.

Another challenging aspect is how to perform TDOA measurements with high accuracy considering that time of arrival measurements are performed at different reference nodes having different reference oscillators. In fact, conventional TDOA estimation requires reference nodes to be time synchronized with uncertainty in the order of 33 ps (corresponding to 1 cm distance estimation error as per requirements) via precise calibration and wired interconnections. To avoid this issue, such tight synchronization requirement has been relaxed to several microseconds through the introduction of a dedicated double cross-correlation algorithm, thus allowing wireless synchronization and easier calibration. The algorithm requires the introduction of an UWB reference transmitter that is used to provide a reference synchronization signal.

Specifically, from a localization point of view, the receivers (indicated as RX₁ and RX₂ in Fig. 20) and the additional transmitting node (i.e., TX₁) are located in known positions (i.e., the propagation delays between TX₁ and the two receivers, indicated as t_{p11} and t_{p12} , are known *a priori*) while only the tag (i.e., TX₂) position is unknown (i.e., the propagation delays indicated as t_{p21} and t_{p22} are the unknown). The TDOA to be estimated is given by $t_{p22} - t_{p21}$.

With reference to Fig. 20, we indicate with t_R the unknown offset between RX₁ and RX₂ (in the order of a few microseconds), with t_1, t_2 the unknown transmission starting instants

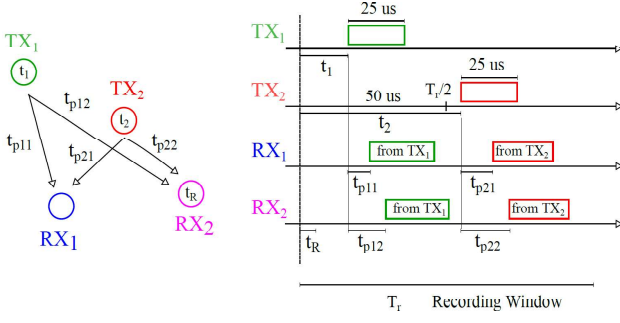


Fig. 20. The double-correlation synchronization scheme.

of TX₁ and TX₂, and with T_r the acquisition window of each receiver (in the order of $100\mu s$). Moreover, we suppose that TX₁ transmits a train of pulses (duration in the order of $25\mu s$) within the first half of the receiver acquisition window while TX₂ transmits a similar train of pulses within the second half, i.e., with $t_2 > T_r/2$. Denote with $s_1(t)$, $s_2(t)$ the transmitted signals emitted by TX₁ and TX₂, respectively. We do not make any assumption on their shape apart from their duration that has to be less than $T_r/2$. Given this configuration and taking the clock of RX₁ as the reference timeline, we can express the received signals at RX₁ in the first and second half of the recording window, respectively, as

$$r_{11}(t) = s_1(t - t_1 - t_{p11}) + n_{11}(t), \quad (4)$$

$$r_{12}(t) = s_2(t - t_2 - t_{p21} + T_r/2) + n_{12}(t), \quad (5)$$

where t_{p11} is the propagation delay from TX₁ to RX₁ (known) and t_{p21} the propagation delay from TX₂ to RX₁ (unknown). Similarly, the received signals at RX₂ are

$$r_{21}(t) = s_1(t - t_1 - t_{p12} - t_R) + n_{21}(t), \quad (6)$$

$$r_{22}(t) = s_2(t - t_2 - t_{p22} + T_r/2 - t_R) + n_{22}(t), \quad (7)$$

where t_{p12} is the propagation delay from TX₁ to RX₂ (known) and t_{p22} the propagation delay from TX₂ to RX₂ (unknown). In both cases $n_{xy}(t)$ represents the thermal noise. At this point we compute the cross-correlation functions of the received signals coming from TX₁ and TX₂ within an integration window of $T_w = T_r/2$ seconds, respectively

$$C_1(t) = \int_{T_w} r_{11}(\tau) r_{21}(t + \tau) d\tau, \quad (8)$$

$$C_2(t) = \int_{T_w} r_{12}(\tau) r_{22}(t + \tau) d\tau. \quad (9)$$

It turns out that

$$\begin{aligned} C_1(t) &= g_1(t - t_{p12} + t_{p11} - t_R) + w_1(t) \\ C_2(t) &= g_2(t - t_{p22} + t_{p21} - t_R) + w_2(t), \end{aligned} \quad (10)$$

where $g_1(t)$, $g_2(t)$ are the auto-correlation functions of $s_1(t)$, $s_2(t)$, respectively. By neglecting the noise, $t_1 = t_{p12} - t_{p11} + t_R$, $t_2 = t_{p22} - t_{p21} + t_R$ are the delays at which the peaks of the cross-correlations are located. Taking the difference between these delays it results

$$\Delta T = t_2 - t_1 = (t_{p22} - t_{p21}) - (t_{p12} - t_{p11}), \quad (11)$$

where $(t_{p12} - t_{p11})$ is known and $(t_{p22} - t_{p21})$ is the TDOA that we aim at estimating. Specifically, the TDOA estimate can be obtained as

$$\text{TDOA} = \Delta T + (t_{p12} - t_{p11}). \quad (12)$$

Obviously, in the presence of noise, the TDOA estimate will be affected by errors. Note that the TDOA in (12) does not depend on the unknown clock offsets t_R , t_1 , and t_2 provided that the received signals fits the two half recording windows of duration T_w each. Such duration has to be designed as a trade-off between the maximum tolerable synchronization offset, the additional accumulated noise (performance degradation), and the computational complexity. In the implemented system, the maximum tolerable offsets are in the order of several microseconds thus allowing an easy synchronization between receivers, even with standard wireless devices.

Large side lobes in the signal correlation-correlation function caused by the periodic nature of the generated sequence of UWB pulses, might confuse the peak detection process (ambiguities), therefore a suitable pseudo-noise (PN) modulation of pulses would be required. Fortunately, the signal generated by the UWB chip is characterized by a strong intrinsic jitter so that the double-correlation estimator exhibits approximately the same performance as that of using a generator with PN modulated pulses, with the advantage of a lower implementation complexity (no modulation needed). This is evident in Fig. 21 where the auto-correlation function (zoomed in the central part) is shown, respectively, for a burst of unmodulated UWB pulses (e.g., $\epsilon_n = 0$ in (1)), PN-modulated UWB pulses, and pulses as measured by the UWB chip.

Results shown in Fig. 22 indicate that with the parameters reported in Table III, the required accumulated (over $N_s = 5,000$ pulses) signal-to-noise ratio (SNR), corresponding to a Root Mean Square Error (RMSE) in TDOA estimate of 33 ps (1 cm distance accuracy), is about 37 dB, which differs by only 1 dB from results one would obtain in theory with a modulated PN sequence. It is worth noticing that the actual SNR per pulse is $10 \log_{10} 5000 = 37$ dB less, which is compatible with the typical link budget computed for UWB signals at a few meters of distance and with a FCC compliant TX power. The plots labeled "single xcorr" refer to performance achievable using a pure TDOA scheme with perfectly synchronized reference nodes, whereas the plots labeled "double xcorr" refer to the performance achievable with the double-correlation scheme proposed above. The adoption of the double cross-correlation scheme does not lead to appreciable differences. As it is evident in Fig. 22, increasing the integration time from $T_w = 50\mu s$ to $T_w = 100\mu s$ is not relevant as it only adds noise to the estimation degrading thus the performance.

VII. PERFORMANCE

A. Wireless Power Transfer Performance

A number of experiments were carried out to characterize the maximum tag operating distance from the UHF energy showers, which is mainly constrained by the quiescent current consumption of the PMU and its minimum input threshold voltage (330mV) required to operate. First, a 2 W-ERP UHF

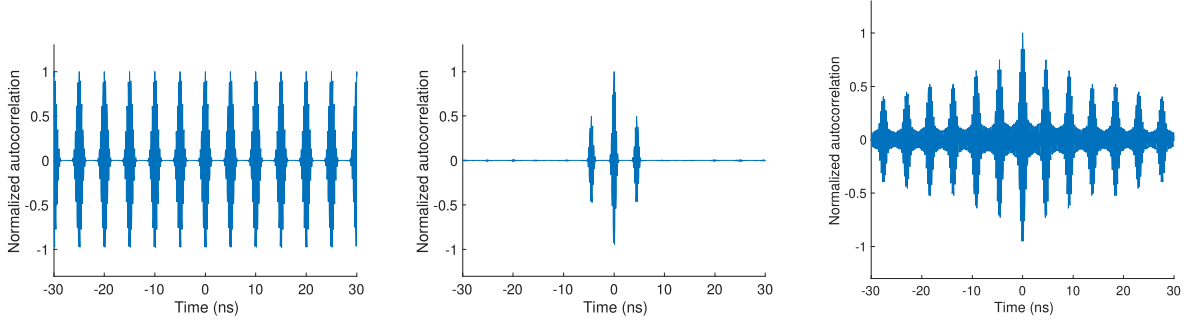


Fig. 21. Auto-correlation function: (left) unmodulated UWB pulses, (center) PN-modulated UWB pulses, (right) measured UWB pulses.

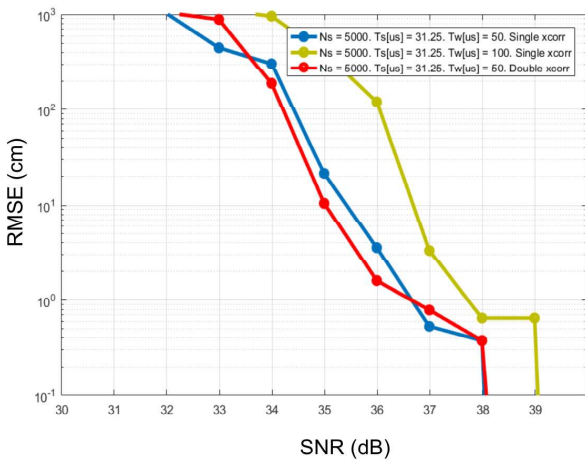


Fig. 22. TDOA RMSE (mapped in cm) as a function of the (accumulated) SNR using experimental data.

TABLE III
MAIN SYSTEM PARAMETERS

Parameter	Value
Tag activation RX power	-13 dBm (first activation) -16 dBm
DC/DC input voltage	> 330 mV
Tag power consumption	< 5 μ W
Tag recharge time	< 200 ms
Tag antenna gain	1.8 dBi
UWB signal center frequency	4 GHz
UWB signal bandwidth	1.4 GHz
UWB TX power density	-50dBm/MHz
UWB pulse repetition period	6.25 ns (with jitter)
Number of UWB pulses	5,000
Reader integration time T_w	31 μ s
Reader RX antenna gain	5 dBi
Reader Noise figure	2 dB

shower was used and a fully discharged tag was subsequently positioned at decreasing distances until the circuit was successfully turned on. The corresponding operating conditions of this first activation were recorded. Once the tag was activated, the distance was increased until the tag stopped operating (see Fig. 23). The above measurement procedure was performed with the PMU shown in Fig. 10, and then with a PMU based on the ASIC described in [29]. As a general result, it was found out that first activation from a discharged state occurs at lower distances because of the high in-rush current occurring

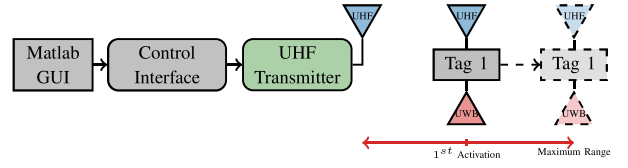


Fig. 23. Wireless power transfer test. The tag is periodically addressed with a GUI developed in Matlab which controls the UHF transmitter, described in Sec. III, through the Control Interface based on Raspberry PI 3 board.

TABLE IV
TAG POWERING AND ACTIVATION RANGE. P_{DC} = POWER AT RECTIFIER OUTPUT, V_{OC} = RECTIFIER OPEN-CIRCUIT VOLTAGE, P_{RX} = RECEIVED POWER AT TAG ANTENNA, D = ACTIVATION DISTANCE.

TX power = 2W ERP	$P_{DC}(\mu W)$	$V_{OC} \text{ min}(V)$	$P_{RX} \text{ (dBm)}$	$D(m)$
LOST tag (off-the-shelf components)				
First activation	15	1.02	-13	9.70
Maximum range	7.5	0.750	-16	10.80
LOST tag with power management replaced by ASIC from UNIBO				
First activation	2.63	0.48	-19.67	17
Maximum range	1.168	0.320	-21.98	22.2

at the start-up of the PMU. Once the PMU is started, its quiescent current decreases to steady-state values, and thus the distance can be increased. Operating distances are reported in Tab. IV, and are more than 10 m with the off-the-shelf PMU and more than 22 m with the custom ASIC (both devices have been equipped with the same single monopole rectenna) which further demonstrates the potential of the technology.

B. Localization performance

The main system parameters considered for testing are shown in Table III. A wide testing campaign to evaluate the localization accuracy has been performed at UCLouvain. A room of size $10 \times 7 \text{ m}^2$, shown in Fig. 24, was used. 2D localization was performed using transmit and receive antennas placed on poles of 2.03 meters high. The receiving antennas were located at the corners of the room and UHF Power Transmit Units were placed at the middle of 3 sides of the room. The exact location of the tag to be localized was recorded using a TOTAL laser station; the accuracy of this measurement is of a few mm. Fig. 25 displays the cumulative error (meters, absolute errors in log scale) for different integration times T_w , ranging from $0.32 \mu\text{s}$ to $82 \mu\text{s}$, by steps of a factor four. $1 \mu\text{s}$ corresponds to an insufficient integration time; integration times larger than

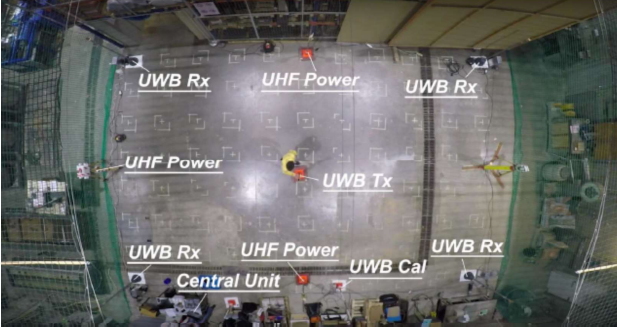


Fig. 24. Room at UCLouvain where experiments have been carried out, seen from top. In white characters, the main components.

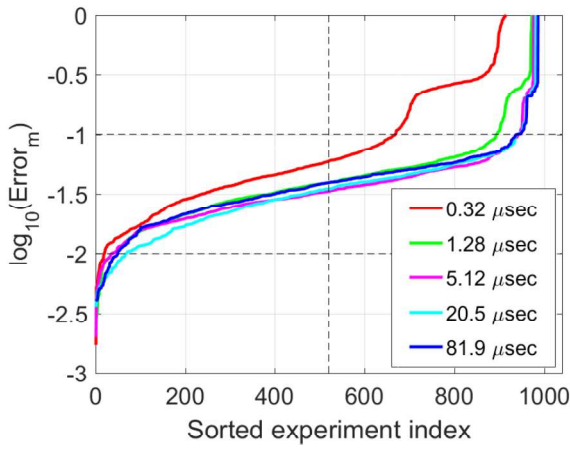


Fig. 25. Cumulative error versus sorted experiment index for different integration times T_w .

$5 \mu\text{s}$ produce similar results, with a median error very close to 3.5 cm. Good robustness to shadowing has been demonstrated with metallic obstacles having a diameter in the order of 40 cm. Directive antennas (with gain near 5 dB, see Fig. 15) have been quite useful to limit false detection resulting from multiple reflections. Nevertheless further research on multipath mitigation, using both hardware and software means, is still worthy.

A final demonstrator of the LOST project was installed and operated at the ESA/ESTEC Robotics Lab premises (see Fig. 26). The demo setup consisted of 4 reference nodes deployed at known positions, 1 UWB reference tag for synchronization, 3 "energy showers", 1 tag mounted on top of the Mars Rover prototype, and 1 tag mounted on a manually handled pole. All nodes were connected to the Control and Central Units, thus resulting in a fully integrated system whose output was visible through the GUI.

To assess the performance, we considered 11 tag positions where 100 measurements were taken each time. The global configuration of the system and 11 positions, recorded with a TOTAL station (i.e. with an accuracy of the order of 2 millimeters) are displayed in Fig. 27-(left). In the following numerical results, we fed the Localization Engine with the measured TDOA data. In the Localization Engine we set the number of location particles to 30,000. Due to physical constraints of the

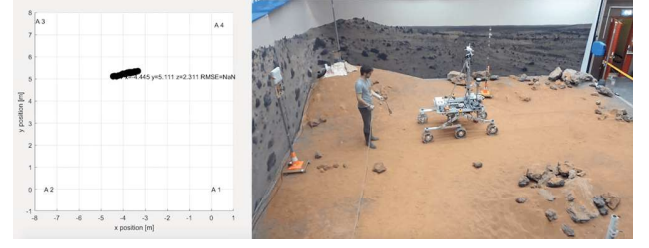


Fig. 26. (Left) Screenshot of the GUI as taken during the demo at ESA/ESTEC (Right) Robotics Lab with the Mars Rover prototype.

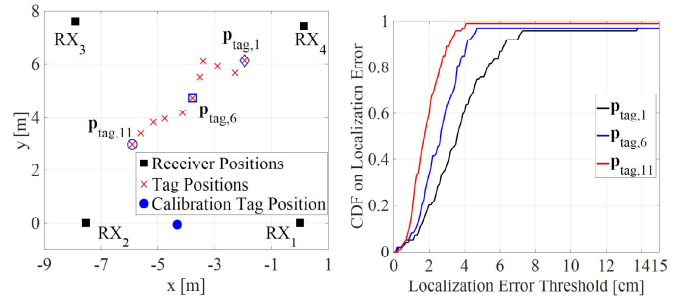


Fig. 27. (Left) Measurement scenario with positions of four receivers (corners), calibration tag (bottom) and 11 test positions of the tag in 2D plane; (Right) Empirical CDF of the localization error in three tag test positions.

demo area, all reference nodes were placed approximatively at the same height thus leading to potential large errors in the z-direction. To avoid that such large errors affect the position estimation, we decided to disable the estimation of the tag's height by forcing it to a a-priori value, which was not always exactly corresponding to the actual height because of the non-regular soil. The resulting error was measured to be below 2.6 cm. In a real set up in which reference nodes can be deployed in the area with less constraints, also the height of the tag can be estimated accurately using the same localization engine.

Among 100 samples, there is from 0 to 7 outliers, which are generally located very far. Assuming that they can be removed using of dedicated clustering algorithms, the achievable performance is close to the one calculated without outliers. Several approaches can be adopted to detect and cluster the outliers. In the presence of one outlier and more than 3 TDOA measurements, one can perform consistency checks by grouping measurements in groups of 3. A complementary approach is to take advantage of the memory during the tracking by checking time-consistencies as measurements cannot suddenly change.

Fig. 27-(right) shows the (empirical) Cumulative Density Function (CDF) of the localization error. For the last tag position (indicated with $p_{\text{tag},11}$), we can see that the localization error is below 2 cm in 50% of the cases. Now we consider the first position (namely, $p_{\text{tag},1}$) which is the one experiencing the outlier effect. The corresponding CDF is shown in Fig. 27-(right) using a continuous black line. Because the number of outliers (three outliers were present in this set-up) is negligible with respect to the total number of measurements, it can be observed that the overall localization error still remains below 10 cm in 95% of cases.

Experiments with $34 \times 34 \text{ cm}^2$ metallic obstacles between transmitter and two of the receivers were also carried out and exhibited good performance. It was also shown that the localization works properly when the tags are placed inside cardboard boxes, i.e. in conditions where optical line-of-sight would not be ensured.

VIII. CONCLUSION

This work describes a localization system using ultra-low power UWB tags developed in the framework of the ESA funded project "LOST" whose purpose was to identify suitable technologies to track floating objects within space stations. Obviously, such a technology also has several potential terrestrial applications, such as in the field of logistics. Despite the stringent requirements imposed by the project, the experimental tests confirmed the possibility to transfer sufficient energy to activate and localize a tag at distances beyond 10 meters, reaching a localization accuracy close to 1 cm (median value near 3.5 cm) over a coverage area of $10 \times 7 \text{ m}^2$.

Current activity is aimed at designing an ASIC solution for the tag in order to reduce its size and improve its performance. Preliminary experimental results have confirmed the possibility to extend the operating range beyond 20 meters. The next step is to integrate such a technology with UHF Gen. 2 RFID in order to ensure backward compatibility and to ease the identification and addressing processes.

ACKNOWLEDGMENT

Authors would like to thank Kjetil Wormnes, Luc Joudrier, and Gianfranco Visentin from ESA for their support during the project. They also thank Pierre Gérard from UCLouvain for his precious help regarding the retrieval of data from the FPGA. Also thanks to Husnain Ali Kayani and Thomas Pairon for their help with antenna production and experiments.

REFERENCES

- [1] R. Miesen, R. Ebel, F. Kirsch, T. Schafer, G. Li, H. Wang, and M. Vossiek, "Where is the tag?" *IEEE Microwave Mag.*, vol. 12, no. 7, pp. 49–63, Dec. 2011.
- [2] L. M. Ni, D. Zhang, and M. R. Souryal, "RFID-based localization and tracking technologies," *IEEE Wireless Communications*, vol. 18, no. 2, pp. 45–51, April 2011.
- [3] M. Liu, H. Wang, Y. Zhang, L. Ma, and N. Wang, "RFID 3-D Indoor Localization for Tag and Tag-Free Target Based on Interference," *IEEE Transactions on Instrumentation and Measurement*, vol. 68, pp. 3718–3732, Oct. 2019.
- [4] S. Siachalou and et al., "Robotic Inventorying and Localization of Rfid Tags, Exploiting Phase-Fingerprinting," *13th European Conference on Antennas and Propagation (EuCAP)*, pp. 362–367, Nov. 2019.
- [5] E. DiGiampaolo and F. Martinelli, "A Robotic System for Localization of Passive UHF-RFID Tagged Objects on Shelves," *IEEE Sensors Journal*, pp. 8558–8568, Oct. 2018.
- [6] D. Dardari, P. Closas, and P. M. Djuric, "Indoor tracking: Theory, methods, and technologies," *IEEE Trans. Veh. Technol.*, vol. 64, no. 4, pp. 1263–1278, April 2015.
- [7] A. R. Jiménez Ruiz and F. Seco Granja, "Comparing Ubisense, Be-Spoon, and DecaWave UWB location systems: Indoor performance analysis," *IEEE Transactions on Instrumentation and Measurement*, vol. 66, no. 8, pp. 2106–2117, Aug 2017.
- [8] D. Dardari, R. D'Errico, C. Roblin, A. Sibille, and M. Z. Win, "Ultrawide bandwidth RFID: The next generation?" *Proc. IEEE*, vol. 98, no. 9, pp. 1570–1582, Sep 2010, special Issue on RFID - A Unique Radio Innovation for the 21st Century.
- [9] R. D'Errico, J. Keignart, and L. Rudant, "Characterization of UWB backscattering propagation for passive tags identification and localization," in *2013 7th European Conference on Antennas and Propagation (EuCAP)*, April 2013, pp. 1909–1913.
- [10] N. Decarli, F. Guidi, and D. Dardari, "Passive UWB RFID for tag localization: Architectures and design," *IEEE Sensors J.*, vol. 16, no. 5, pp. 1385–1397, March 2016.
- [11] D. Arnitz, U. Muehlmann, and K. Witrisal, "UWB ranging in passive UHF RFID: Proof of concept," *IEEE Electronics Lett.*, vol. 46, no. 20, pp. 1401–1402, Oct. 2010.
- [12] J. Aleksandravicius, N. Decarli, A. Guerra, and D. Dardari, "High-accuracy localization of backscattering UWB tags: Implementation and experimental results," in *2017 IEEE International Conference on RFID Technology Application (RFID-TA)*, Sept 2017, pp. 34–39.
- [13] R. D'Errico and et al., "An UWB-UHF semi-passive RFID system for localization and tracking applications," in *IEEE International Conference on RFID-Technology and Applications, (RFID-TA 2012)*, Nice, France, Nov. 2012, pp. 18–23.
- [14] D. Dardari, N. Decarli, A. Guerra, and F. Guidi, "The future of Ultra-Wideband localization in RFID," in *2016 IEEE International Conference on RFID (RFID) (IEEE RFID 2016)*, Orlando, USA, May 2016.
- [15] A. Costanzo and et al., "Energy autonomous UWB localization," *IEEE Journal of Radio Frequency Identification*, vol. 1, no. 3, pp. 228–244, Sept 2017.
- [16] N. Decarli and D. Dardari, "Time domain measurements of signals backscattered by wideband RFID tags," *IEEE Transactions on Instrumentation and Measurement*, vol. 67, no. 11, pp. 2548–2560, Nov 2018.
- [17] D. Dardari et al., "An ultra-wideband battery-less positioning system for space applications," in *2019 IEEE International Conference on RFID Technology and Applications (RFID-TA)*, Sep 2019, pp. 1–6.
- [18] F. Keshmiri, R. Chandra, and C. Craeye, "Design of a UWB antenna with stabilized radiation pattern," in *2008 IEEE Antennas and Propagation Society International Symposium*, July 2008, pp. 1–4.
- [19] A. Jazairli and Flandre, "A 65 nm cmos ultra-low-power impulse radio ultrawideband emitter for short-range indoor localization," *Journ. Low Power Electron.*, vol. 11, no. 3, pp. 349–358, Sep. 2015.
- [20] P. Gerodez and C. Craeye, "Reduced-order pattern representation of UWB antenna devoted to positioning," in *Proc. 3d European Conf Antennas Propagat., Berlin, Germany*, March 2009.
- [21] M. Fantuzzi, D. Masotti, and A. Costanzo, "A novel integrated uwb-uhf one-port antenna for localization and energy harvesting," *IEEE Transactions on Antennas and Propagation*, vol. 63, no. 9, pp. 3839–3848, Sep. 2015.
- [22] M. Fantuzzi, G. Paolini, M. Shanawani, A. Costanzo, and D. Masotti, "An orientation-independent uhf rectenna array with a unified matching and decoupling rf network," *International Journal of Microwave and Wireless Technologies*, vol. 11, no. 5-6, p. 490–500, 2019.
- [23] U. Olgun, C. Chen, and J. L. Volakis, "Investigation of rectenna array configurations for enhanced rf power harvesting," *IEEE Antennas and Wireless Propagation Letters*, vol. 10, pp. 262–265, 2011.
- [24] M. Fantuzzi, M. Del Prete, D. Masotti, and A. Costanzo, "Quasi-isotropic RF energy harvester for autonomous long distance IoT operations," in *2017 IEEE MTT-S International Microwave Symposium (IMS)*, June 2017, pp. 1345–1348.
- [25] N. Decarli, M. D. Prete, D. Masotti, D. Dardari, and A. Costanzo, "High-accuracy localization of passive tags with multisine excitations," *IEEE Transactions on Microwave Theory and Techniques*, vol. 66, no. 12, pp. 5894–5908, Dec 2018.
- [26] V. Rizzoli, A. Costanzo, D. Masotti, P. Spadoni, and A. Neri, "Prediction of the end-to-end performance of a microwave/rf link by means of non-linear/electromagnetic co-simulation," *IEEE Transactions on Microwave Theory and Techniques*, vol. 54, no. 12, pp. 4149–4160, Dec 2006.
- [27] D. Fabbri, M. Pizzotti, and A. Romani, "Micropower design of an energy autonomous rf tag for uwb localization applications," in *2018 IEEE International Symposium on Circuits and Systems (ISCAS)*, May 2018, pp. 1–5.
- [28] M. Magno, V. Jelicic, B. Srbinovski, V. Bilas, E. Popovici, and L. Benini, "Design, implementation, and performance evaluation of a flexible low-latency nanowatt wake-up radio receiver," *IEEE Trans. Ind. Informatics*, vol. 12, no. 2, pp. 633–644, Apr. 2016.
- [29] M. Dini, A. Romani, M. Filippi, and M. Tartagni, "A nano-current power management IC for low voltage energy harvesting," *IEEE Trans. Power Electron.*, vol. 31, no. 6, pp. 4292–4304, 2016.
- [30] N. Agrawall, C. Kumar, and K. Ray, "Wide-band planar monopulse antenna," *IEEE Transactions on Antennas and Propagation*, vol. 46, no. 2, pp. 294–295, Feb 1998.

- [31] Federal Communications Commission, "Revision of part 15 of the commission's rules regarding ultra-wideband transmission systems, first report and order (ET Docket 98-153)," Adopted Feb. 14, 2002, Released Apr. 22, 2002.
- [32] A. Mallat, S. Gezici, D. Dardari, C. Craeye, and L. Vandendorpe, "Statistics of the mle and approximate upper and lower bounds—part i: Application to toa estimation," *IEEE Transactions on Signal Processing*, vol. 62, no. 21, pp. 5663–5676, 2014.